Clim Dyn (2013) 41:787–802
DOI 10.1007/s00382-012-1472-3

Midlatitude storms in a moister world: lessons from idealized baroclinic life cycle experiments

James F. Booth · Shuguang Wang · Lorenzo Polvani

Received: 23 April 2012 / Accepted: 23 July 2012 / Published online: 7 August 2012

Abstract The response of midlatitude storms to global warming remains uncertain. This is due, in part, to the competing effects of a weaker meridional surface temperature gradient and a higher low-level moisture content, both of which are projected to occur as a consequence of increasing greenhouse gases. Here we address the latter of these two effects, and try to elucidate the effect of increased moisture on the development and evolution of midlatitude storms. We do this with a set of highly controlled, baroclinic lifecycle experiments, in which atmospheric moisture is progressively increased. To assess the robustness of the results, the moisture content is changed in two different ways: first by using different initial relative humidity, and second by varying a parameter that we insert into the Clausius-Clapeyron equation. The latter method allows us to artificially increase the moisture content above current levels while keeping the relative humidity constant. Irrespective of how moisture is altered, we find that nearly all important measures of storm strength increase as the moisture content rises. Specifically, we examine the storm's central pressure minimum, the strongest surface winds, and both extreme and accumulated precipitation rates. For all these metrics, increased moisture yields a stronger storm. Interestingly, we also find that when moisture is increased beyond current levels, the resulting storm has a reduced horizontal scale while its vertical extent increases. Finally, we note that for moisture increases comparable to those projected to occur by the end of the twentyfirst century, the actual amplitude of the increases in storm strength is relatively modest, irrespective of the specific measure one uses.

Keywords Midlatitude storms · Baroclinic · Life cycles · Global warming · Moisture

J. F. Booth (✉)
NASA Goddard Institute for Space Studies,
2880 Broadway, New York, NY 10025, USA
e-mail: jbooth.atmos@gmail.com

S. Wang · L. Polvani
Department of Applied Physics and Applied Mathematics,
Columbia University, 500 West 120th Street, Rm. 290,
New York, NY 10027, USA

L. Polvani
Department of Earth and Environmental Sciences, Lamont Doherty Earth Observatory, Columbia University, S. W. Mudd Bldg., Rm. 216, Mail Code 4701, New York, NY 10027, USA

1 Introduction

Synoptic storms are the dominant weather events in midlatitude winter, and are often accompanied by heavy precipitation and strong winds. They are also a critical component of the hydrological cycle, at both global and regional scales. In the coming decades, atmospheric temperatures are expected to rise due to increased greenhouse gas concentrations (Solomon et al. 2007). This global warming trend will inevitably create changes in the midlatitudes. However, the precise impact of global warming on midlatitude storms remains, at present, highly uncertain.

General Circulation Model (GCM) projections suggest two mechanisms affecting the strength of midlatitude storms with global warming: the equator-to-pole surface temperature gradient will decrease (Solomon et al. 2007), and the moisture content of the atmosphere will increase (Held and Soden 2006). Unfortunately, these two mechanisms will have opposing impacts on storm strength. On the one hand, a decrease in the meridional gradient of surface temperatures will weaken the baroclinicity of the

lower troposphere, weakening an important source of available potential energy for midlatitude storms (e.g., Holton 2004, Ch. 8). On the other hand, an increase in low-level moisture will increase the energy associated with latent heat release during storm development (e.g., Carlson 1998, pp. 216–217, or Martin 2006, pp. 290–295). The presence of two opposing mechanisms makes the assessment of projected storm strength difficult, as we now briefly review.

First, recent analyses of midlatitude storms using model output from GCMs run under global warming scenarios, have reported contradictory results as to the changes in extreme storm events in the future climate. Independent studies using the Max-Plank GCM (Bengtsson et al. 2009) and the Hadley Centre GCM (Catto et al. 2011), found no increase in the frequency or strength of extreme storms (based on the relative vorticity at 850 hPa). In contrast, an analysis that examined all of the GCMs from the World Climate Research Programme's (WCRP's) Coupled Model Intercomparison Project phase 3 (CMIP3) argued that the number of extreme midlatitude storms will increase with global warming (Lambert and Fyfe 2006). However, the storm strength metric used in the latter study, sea level pressure (SLP) minimum, may have introduced a bias. This is because the climatological SLP is lower near the poles, and therefore, a poleward shift in storm track location can increase the frequency of deep storms, even if the storms' circulations are not actually stronger (Ulbrich et al. 2009). In addition, other studies of the CMIP3 models found that the number of extreme wind events (Gastineau and Soden 2009) and the extreme precipitation (O'Gorman and Schneider 2009) in the midlatitudes increases with global warming. Both types of events typically occur within midlatitude storms, although a direct attribution cannot be made from these studies.

In addition to these differences, one might be concerned as to the ability of GCMs to faithfully capture the moist evolution of midlatitude storms, in terms of both the dynamics and thermodynamics, and these concerns raise some doubts about GCM projections of the response of midlatitude storms to moisture changes. A comparison of one CMIP3 GCM to cloud satellite observations found that the GCM had a low bias in its upper-level clouds within midlatitude storms (Naud et al. 2010), which implies a weak vertical moisture transport in the model. In addition to model physics, the typical resolution of current GCMs is also a common concern. In the studies mentioned above, Bengtsson et al. (2009) and Catto et al. (2011) used modified GCMs with a spatial resolution of 63 km, which is finer than that of the CMIP3 models. However, typical weather forecasting models are usually integrated with a finer horizontal grid spacing, so as to properly resolve midlatitude storm's frontal dynamics. Therefore, the ability of GCMs to properly capture the moist evolution of midlatitude storms remains an open question. Indeed, Champion et al. (2011) and Li et al. (2011) found that the strength of the most extreme storms, in terms of surface winds and precipitation, increases when the horizontal resolution is increased from 100 to 25 km.

Second, a different line of research has been probing the dynamics of baroclinic life cycles, going back to the late 1970's. Most of these early studies were carried out in a very simplified context, notably in the absence of moisture (e.g., Simmons and Hoskins 1978; Rotunno et al. 1994; Thorncroft et al. 1993). Later work has included moist physics, and it has become clear that moist processes can greatly influence storm dynamics. Using a theoretical framework, Emanuel et al. (1987) found that moisture reduces gross static stability and strengthens baroclinic eddies. Including moisture also leads to a contraction of the region of vertical motion (Emanuel et al. 1987; Fantini 1993). Numerical modeling studies have shown that the presence of moisture leads to stronger storms and faster development (Gutowski et al. 1992; Mak 1994; Whitaker and Davis 1994). Only one study of lifecycle response to changes from dry to full moist conditions (Pavan et al. 1999) reported that moisture has little impact on eddy kinetic energy (EKE). In contrast, more recent studies have shown a large difference in strength between dry and moist lifecycles (Boutle et al. 2010, 2011, hereafter B2011).

More specifically, Boutle and collaborators found that storm EKE grows as the initial moisture content is increased. In experiments in which the initial conditions were varied from zero relative humidity (RH) to RH close to observations, the storm EKE increased by 100 % (Boutle et al. 2010). B2011 also confirmed the importance of the warm conveyor belt (WCB, e.g., Wernli and Davies 1997; Carlson 1998, pp. 302–319) in ventilating moisture out of the planetary boundary layer (PBL). B2011 also corroborated the notion, put forth in earlier case-studies, that latent heating associated with rising moist air influences storm strength (e.g.,, Davis et al. 1993; Stoelinga 1996; Booth et al. 2012; Campa and Wernli 2012), and showed that the amount of heating increases as the initial RH is increased. Finally, they showed that a tight relationship exists between the ventilation of moisture out of the boundary layer and the precipitation that falls under the WCB.

The objective of this paper is to independently reproduce and extend the B2011 study: here we focus, specifically, on the impact of moisture on midlatitude storms. Our goal is to systematically explore how storms change with increasing moisture content, as projected under global warming, using the idealized baroclinic life cycle experiments. One way to accomplish this is to simply modify the initial relative humidity. Therefore, in a first experiment,

we examine a set of integrations in which the initial RH is progressively increased from dry to moist, as in B2011. These experiments are meant to help clarify the impact of moisture, which appeared to be different in the studies by Pavan et al. (1999) and B2011.

As an alternative approach, we also employ the method used in Frierson et al. (2006), whereby the moisture content of the atmosphere is changed by artificially altering the definition of the saturation vapor pressure. This is accomplished by introducing an artificial coefficient in the Clausius-Clapeyron equation, and changing the coefficient so as to alter the moisture content of the atmosphere in a progressive way, while the initial RH is held constant. An experiment of this type might be more relevant to global warming projections, because GCMs and theory predict that the change in RH with global warming will be small (as summarized in Sherwood et al. 2010). We present the results of this experiment below, and show that they confirm the conclusions reached by increasing initial RH.

Needless to say, it is also possible to change the moisture content of the atmosphere by varying the initial temperature. However, that approach requires a number of choices with respect to treatment of the meridional and vertical temperature gradients, as well as the height of the tropopause, all of which may impact the storm's response in complex ways (e.g., Lorenz and DeWeaver 2007; O'Gorman 2011). Therefore, we are setting those experiments aside for a separate study, and here deal with the simpler questions of moisture increase without temperature changes

Perhaps the key novelty of this paper is that we here use a wide variety of metrics to examine the storms' response to increasing moisture. Part of the present confusion in the literature stems from the fact that different authors have focused on different metrics (e.g., pressure vs. winds), which makes it difficult to compare the studies. Here we go well beyond the traditional EKE, and document baroclinic life cycle changes in several important aspects: some are more traditional, like the central pressure minimum (widely used in the synoptic weather community), while others emphasize the storm impacts (such as surface winds and extreme precipitation).

This paper is divided into the following sections. Section 2 describes the numerical model, the experimental setup, and the storm metrics used in this study. The results are reported in Sect. 3, which is separated into 3 experiments: the first focuses on storm sensitivity to initial RH as in B2011, the second on storm sensitivity to changing the moisture content from dry to current levels, and the third reports on the sensitivity to changing moisture from current to two times current moisture conditions. Section 4 is a discussion of two specific issues, and Sect. 5 offers a summary and some conclusions.

2 Methods

In this paper, unlike many of the classic studies of idealized baroclinic life cycles, we use a numerical model with "full physics", i.e., a realistic boundary layer scheme, parameterized cumulus convection, cloud microphysics, and surface moisture and heat fluxes. Nonetheless, we wish to retain the flavor of the earlier studies, notably their simplicity and reproducibility. In that spirit, we have (1) implemented analytically specified initial conditions for both the dynamical variables and water vapor and (2) we have adopted a freely available and very widely used (non-proprietary) model. In this section we include: first the details of our model, then the initial conditions we have adopted, and finally the different metrics that will be used in later sections to describe the storms.

2.1 The model

We here use the Weather Research and Forecast (WRF) (Skamarock et al. 2008) model version 3.0.1. WRF solves the non-hydrostatic primitive equations and is configured as a channel: the east and west boundaries are periodic, and the north and south boundaries are symmetric. Near the model top, vertically propagating gravity waves are absorbed with a 5 km-thick layer with an implicit damping scheme, which prevents unphysical wave reflection. The horizontal and vertical advection schemes are 5th order and 3rd order accurate, respectively. Moisture and other scalars are advected using a positive definite scheme (Skamarock et al. 2008).

The channel is taken to be on the Cartesian plane with constant Coriolis parameter $f = 10^{-4}\ \mathrm{s}^{-1}$, corresponding to 45° latitude. Unless otherwise specified, the model domain has 81 × 181 × 50 grid points in the x, y and z directions, with horizontal grid spacing (DX) equal to 50 km. This corresponds to a cubic domain of $4{,}000 \times 9{,}000 \times 23\ \mathrm{km}^3$, roughly 81 degrees of latitude by 51 degrees of longitude. To test sensitivity to model resolution, we also carry out integrations using DX = 25, 100 and 200 km, while maintaining the same physical domain size. For the parameterization schemes, we opt for those which are widely used in the weather forecasting community. Cumulus convection is parameterized using the Kain-Fritsch (KF) scheme (Kain and Fritsch 1993). Boundary layer turbulence and vertical sub-grid scale eddy diffusion are treated with the YSU scheme (Hong et al. 2006); this is a first order closure scheme that includes a non-local counter gradient transport. Horizontal sub-grid eddy mixing is parameterized using the 2D Smagorinsky first order closure scheme, performed in physical space. Surface moisture and heat fluxes are parameterized following Monin–Obukhov similarity theory. The bulk

microphysics scheme is the Purdue-Lin scheme (Lin et al. 1983; Chen and Sun 2002). This scheme has six species: water vapor, cloud water, cloud ice, rain, snow and graupel. No radiation is included in our model integrations.

Finally we note that, unlike most traditional life cycle experiments but following B2011, the lower boundary condition is treated here as a sea surface. Therefore, it acts as a source and sink of sensible heat and moisture, as well as momentum. The sea surface temperature is chosen to be time-independent, and is set to be 0.5 °C smaller than the initial atmospheric temperature at the lowest model level.

2.2 The experiments

All of the integrations presented in this paper use identical initial conditions for temperature (T) and zonal wind ($\mathbf{u}$), similar to those in Polvani and Esler (2007), except that our initial jet is placed on an f plane with Cartesian geometry, as in Wang and Polvani (2011). These initial conditions yield winds that are similar to the observed midlatitude jets, while remaining balanced and simple enough to be described analytically. To initiate the life cycle we apply a finite amplitude perturbation (1 K) to the temperature field at all model levels, as in Polvani and Esler (2007). Because we are not initializing the life cycle with normal modes, the instability takes several days to reach the mature stage.

As already mentioned, this paper reports on three sets of numerical experiments, each consisting of 6 integrations. The first set of integrations attempts to reproduce the results of B2011. To do this, we perform integrations with different initial relative humidity (RH), but identical winds and temperature. In these integrations, the initial RH is given by:

$$RH = RH_0 * \begin{cases} (1 - 0.85 * Z/Z_T)^{1.25} & \text{for } Z \le Z_T \\ 0.15 \quad \text{for } Z > Z_T \end{cases} \qquad (1)$$

Z_T, the moisture scale height, equals 12 km. This formula is very similar to the one used ion B2011, with RH_0 being the key parameter to be varied. Note that, in our case, the initial RH varies only with height, whereas B2011 and Pavan et al. (1999) used initial RH that varies with both height and latitude. We chose not to include a latitudinal dependence for simplicity. This analytical RH distribution appears to have originated in Weisman and Klemp (1982).

The RH_0 values in the six integrations of Experiment 1 are: 0, 0.2, 0.4, 0.6, 0.8 and 0.95. We have not included the value RH = 1.0, because it generates a rather strange storm, having to do with some peculiar behavior of the cumulus scheme. There are two characteristics of the integrations in Experiment 1 we wish to emphasize. First, in all of the experiments in which we vary RH_0, moisture enters the atmosphere at the lower boundary via evaporation from the sea surface. Thus, the $RH_0 = 0$ integration is only dry at the onset, but moisture enters the atmosphere as the lifecycle evolves. Second, the integration in Experiment 1 with $RH_0 = 0.8$ will be considered the "reference" integration, as it corresponds to conditions most similar to those in observations, and will be referred to with that term hereafter.

In fact, for the second and third sets of integrations we set $RH_0 = 0.8$, and alter the moisture content by changing the saturation vapor pressure definition. This approach tests the sensitivity to moisture in a manner that is relevant to global warming, as documented in the IPCC AR4 projections (e.g., Sherwood et al. 2010), since it allows us to keep RH fixed while increasing water vapor in the atmosphere. Following Frierson et al. (2006), we modify the Clausius-Clapeyron equation by multiplying the saturation pressure of water at its triple-point by a coefficient, C_{SVP}, so that:

$$q_{SAT}(T) = C_{SVP} * 6.11 * e^{\left(\frac{L_v}{R_v} * \left(\frac{1}{273} - \frac{1}{T}\right)\right)} \qquad (2)$$

where L_v is the latent heat of vaporization, R_v is the gas constant of water vapor, and T is temperature. When $C_{SVP} = 1$, $q_{SAT}(T)$ corresponds to the relationship observed in nature, and the model's moisture content is equal to the reference case in Experiment 1.

The second set of integrations, Experiment 2, is an analog to the RH_0 experiment, and consists of six integrations with C_{SVP} set to values from 0 to 1, in increments of 0.2. When $C_{SVP} < 1.0$, the saturation vapor pressure for any given temperature is less than the current conditions. Since we initialize all integrations in this experiment with an identical RH profile, using $C_{SVP} < 1.0$ causes the actual vapor pressure to be less than current conditions. For $C_{SVP} = 0.0$, the water vapor is set zero at all times (so the model is entirely dry).

A third and final set of integrations, Experiment 3, consists of six integrations with C_{SVP} ranging from 1 to 2 in increments of 0.2. This experiment seeks to shed light on how increases in moisture content beyond the current amount will impact the development and intensity of midlatitude storms. Table 1 summarizes the 3 sets of integrations.

Table 1 Experiment details

	Initial relative humidity RH_0 (see Eq. 1)	Moisture content parameter C_{SVP} (see Eq. 2)
Experiment 1	[0.0, 0.2, 0.4, 0.6, 0.8, 0.95]	1.0
Experiment 2	0.8	[0, 0.2, 0.4, 0.6, 0.8, 1]
Experiment 3	0.8	[1, 1.2, 1.4, 1.6, 1.8, 2]

2.3 The metrics

As mentioned in the introduction, part of the current confusion as to the impact of global warming on midlatitude storms can be traced to the fact that different studies have been using different metrics to define the strength of the storms [e.g., the relative vorticity in Bengtsson et al. (2009), or extreme wind in Gastineau and Soden (2009)]. In light of this, we decided to offer a comprehensive view of the storms in our paper, so as to capture most of the important aspects.

To this end, our analysis will focus on five metrics: (1) the eddy kinetic energy (EKE); (2) the storm central pressure minimum; the strongest 99th percentile of (3) the surface wind speed and (4) the precipitation rates; and (5) the accumulated precipitation. The first metric, EKE is the traditional metric reported in life cycle studies (e.g., Simmons and Hoskins 1978). The second metric, the central pressure minimum at sea level, is typically used to track the path of storms, and captures a vertically integrated response of the atmosphere. The strongest surface winds and precipitation are included because they are of great interest for the extreme events that midlatitude storms can produce.

We calculate the metrics as follows. The EKE is calculated from a volume integral of the mass weighted eddies, where the eddies are with respect to the zonal mean. The storm central pressure metric (CTR_PRES) is defined as the minimum sea level pressure within the entire domain; simply finding the minimum suffices, because SLP is a smooth spatial field. On the other hand, the surface winds (WIND99) can include large outliers for their maxima. Therefore, we use the value at the largest 99th percentile to capture the extreme winds, which we calculate using a distribution of the instantaneous winds over the whole domain at each output interval. For these three metrics (EKE, CTR_PRES and WIND99), we analyze output at 12-h intervals.

For the precipitation, we consider two metrics: (1) the strongest 99th percentile of hourly accumulated precipitation rates, and (2) the total accumulated precipitation over the full baroclinic life cycle. For the latter, we output the accumulated precipitation hourly, and calculate the rates from the differences between successive values. Then, for each hourly rate, the top 99th percentile is calculated using all points in the domain. When plotting the rates, we only show the results every 12 h, so as to minimize the noisiness of the plots. Furthermore, we consider separately the rates for the large-scale scale and cumulus scheme precipitation, denoted $\mathrm{PRCP99_{LS}}$ and $\mathrm{PRCP99_{CU}}$, respectively. This is partly motivated by the result of B2011, who show that WCB precipitation is dominated by the large-scales, while cumulus precipitation mostly occurs south of the WCB. For the comparison of the precipitation from runs with different grid size (DX), we reduce all of the output to the 200-km grid to ensure a like-for-like comparison of the precipitation rates across the different DX values.

For the second precipitation metric, we define the total accumulated precipitation as the large-scale plus convective precipitation from day 0 to day 12, averaged over the model domain. We present the results for this metric in the discussion section, to better compare the different experiments.

Finally, for some of these fields the maximum or minimum value over the entire life cycle is of interest. This is denoted with the subscripts "MAX" or "MIN". So, for instance, the minimum central pressure over the entire lifecycle is labeled $\mathrm{CTR\_PRES_{MIN}}$.

3 Results

Before reporting on the effect of moisture on baroclinic lifecycles, we describe the evolution of our reference integration, for which the two key parameters take the values $\mathrm{RH_0} = 0.8$ and $\mathrm{C_{SVP}} = 1$. In Fig. 1, we show the precipitation (color) and SLP (black contours) as the life cycle evolves from 1/4 $\mathrm{EKE_{MAX}}$ on day 6.5 (panel a), to near 1/2 $\mathrm{EKE_{MAX}}$ on day 8 (panel b), and onto $\mathrm{EKE_{MAX}}$ on day 9.5 (panel c). To display the large-scale and cumulus precipitation on the same figure, we multiply the cumulus precipitation rate by -1. There is some small overlap in the location of the cumulus and large-scale precipitation, so the cumulus overlay may be covering over large-scale precipitation.

As one can see in Fig. 1, the storm in our reference integration develops with a structure that is typical of midlatitude storms, as evidenced by the spatial distributions of the SLP and the precipitation in Fig. 1. The region with the strongest precipitation rates (dark red) is found between 35° and 50°, approximately 5 degrees east of the dashed green line in Fig. 1b; this is a region between the cyclone's cold and warm fronts, in which a large amount of condensation occurs. As discussed in the introduction, the moist processes in this region affect the storm strength through diabatic heating (e.g., Davis et al. 1993).

The green curve in Fig. 2a shows the EKE of the reference baroclinic life cycle in Fig. 1. The storm begins its exponential growth on day 4.5 of the integration, and attains its maximum strength on day 9.5, after which it begins to decay. The length of time it takes our storm to develop is a typical duration for a baroclinic life cycle (e.g., B2011).

3.1 Experiment 1: varying $\mathrm{RH_0}$

Having established the reference integration, we now consider how varying the initial relative humidity, $\mathrm{RH_0}$ (as

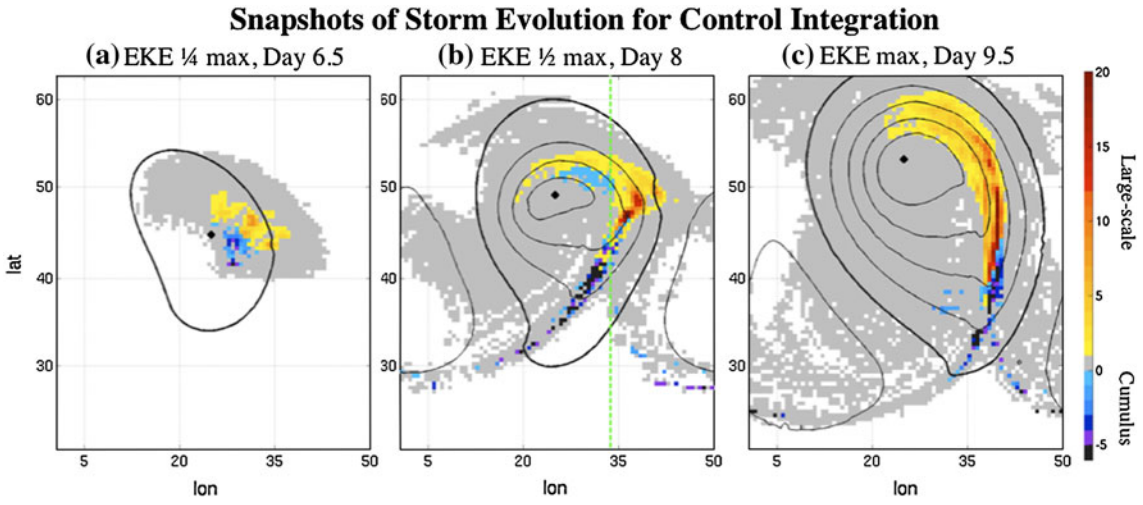

Fig. 1 Sea level pressure contours (*black*) and precipitation rate (*color*) for the integration with $RH_0 = 0.8$. The storm is shown at times relative to its EKE_{MAX}: ¼ max, day 6.5 (**a**), ½ max, day 8 (**b**), and max, day 9.5 (**c**). SLP contours increase monotonically outwards from the storm center, contour interval: 10 hPa. The thickest contour is 1,000 hPa. The *dashed green line* in (**b**) helps identify the WCB (see text). Precipitation generated by the cumulus scheme is plotted as negative. Precipitation units: mm/hour. The figures are zoomed in on the storm circulation instead of showing the full model domain. The ordinate and abscissa have been labeled with the latitude and longitude equivalent to the grid size

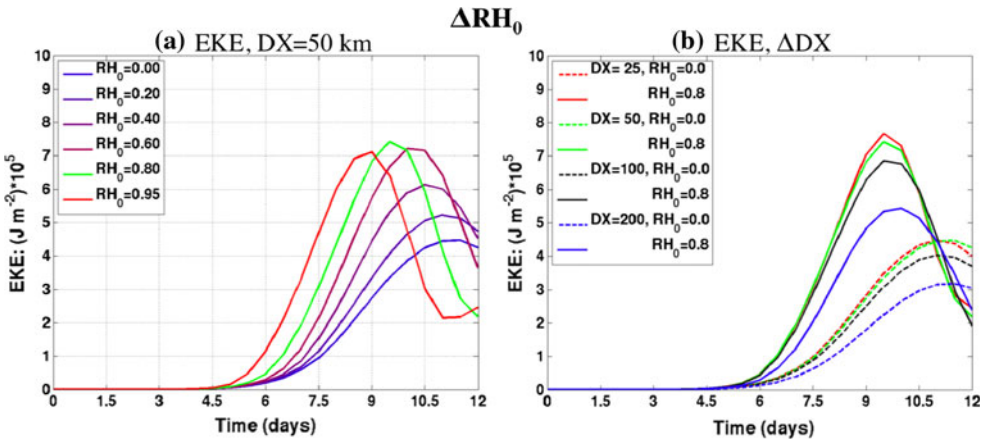

Fig. 2 Time evolution of EKE for the RH_0 experiment (**a**) and the integrations with different grid spacing (**b**). In *both panels* the *solid green line* shows the reference integration. In (**a**), *blue* is the lowest and *red* is the highest RH_0. In (**b**), the *solid curves* show the $RH_0 = 0.8$ cases and the *dashed curves* show the cases with $RH_0 = 0$. Units for EKE: 10^5 J/m^2

shown in Eq. 1), affects the evolution of the baroclinic life cycle. For simplicity, we will refer to this set of integrations as Experiment 1 (cf. Table 1). One goal of this experiment is to validate results reported in B2011: we here use a very different model and set of parameterizations, so it is not a priori obvious how robust the results to B2011 might be, especially in view of the well known sensitivity of convective parameterizations. We also wish to extend their results, by analyzing a larger set of metrics of the storm response to increased relative humidity.

To start, let us consider the EKE time-series for each RH_0 value, from 0 to 0.95. First, it is clear that EKE_{MAX} increases with RH_0 (Fig. 2a). Second, we note that the EKE grows faster as RH_0 is increased. The key point of this figure is that the EKE dependence on initial RH is the same as that reported by Boutle et al. (2010) and B2011, including the small changes in EKE for $RH_0 > 0.6$, and no apparent change for $RH_0 > 0.8$. Hence, the results of those studies are here independently reproduced.

The physical mechanism through which moisture affects storm strength has been discussed in previous case studies (e.g., Reed et al. 1993; Stoelinga 1996), and we only summarize it here for completeness: higher initial RH allows the rising air within the storm to saturate earlier and in greater abundance. This increases the diabatic heating in vicinity of the cyclone center, which strengthens the vertical gradient of the diabatic heating, generating a positive anomaly in low-level potential vorticity, which leads to a faster and stronger storm development. An upper-level, negative PV anomaly associated with the latent heat release is also present (e.g., Martin 2006, pp. 294–300): however, its impact is secondary, and therefore we do not discuss it here.

Having validated previous results, we now address the question of sensitivity to horizontal resolution. Several versions of the same experiment, i.e., with RH_0 varying from 0 to 0.95, were carried out at coarser (DX = 100 and 200 km) as well as finer (DX = 25 km) resolution. The results are presented in Fig. 2b. To keep the figure readable we only show two cases for each resolution: $RH_0 = 0.0$, the driest member of the set, and $RH_0 = 0.8$, the reference case already discussed. Different colors denote different resolutions; the solid curves show the reference case, while dashed curves show the driest case. Two points are worth noting: first, one sees a convergence of the EKE maximum near DX = 50 km. Second, comparing the dashed and solid curves of the same color, one sees that in all cases the reference storm is stronger than the one initialized with $RH_0 = 0.0$, regardless of the horizontal grid-size. Furthermore, for each DX, the change in EKE with RH_0 is qualitatively identical to those with DX = 50 km (not shown). This clearly demonstrates that the strengthening of the storm's EKE with increased water vapor content is a robust result. We also examined the sensitivity of the results to changes in the vertical resolution (not shown), and again found similar behavior.

Beyond EKE, we now wish to report on the effect of increasing the initial RH on other characteristics of a developing storm. In Fig. 3, we discuss the: storm central pressure (CTR_PRES) and the strongest 99th percentile for surface wind speed (WIND99). Consider first Fig. 3a: it is clear that the minimum pressure over the entire lifecycle deepens gradually and monotonically from ~961 to ~951 hPa as RH_0 increases from zero to 0.95. Thus, the central pressure responds to moisture increases in a manner similar to EKE, except that at large RH_0 the EKE_{MAX} appears to saturate, whereas the storm CTR_PRES continues to deepen.

Note that the difference for CTR_PRES_{MIN} between $RH_0 = 0$ and 0.8 is about 10 hPa, which is smaller than changes reported by previous case studies in which the

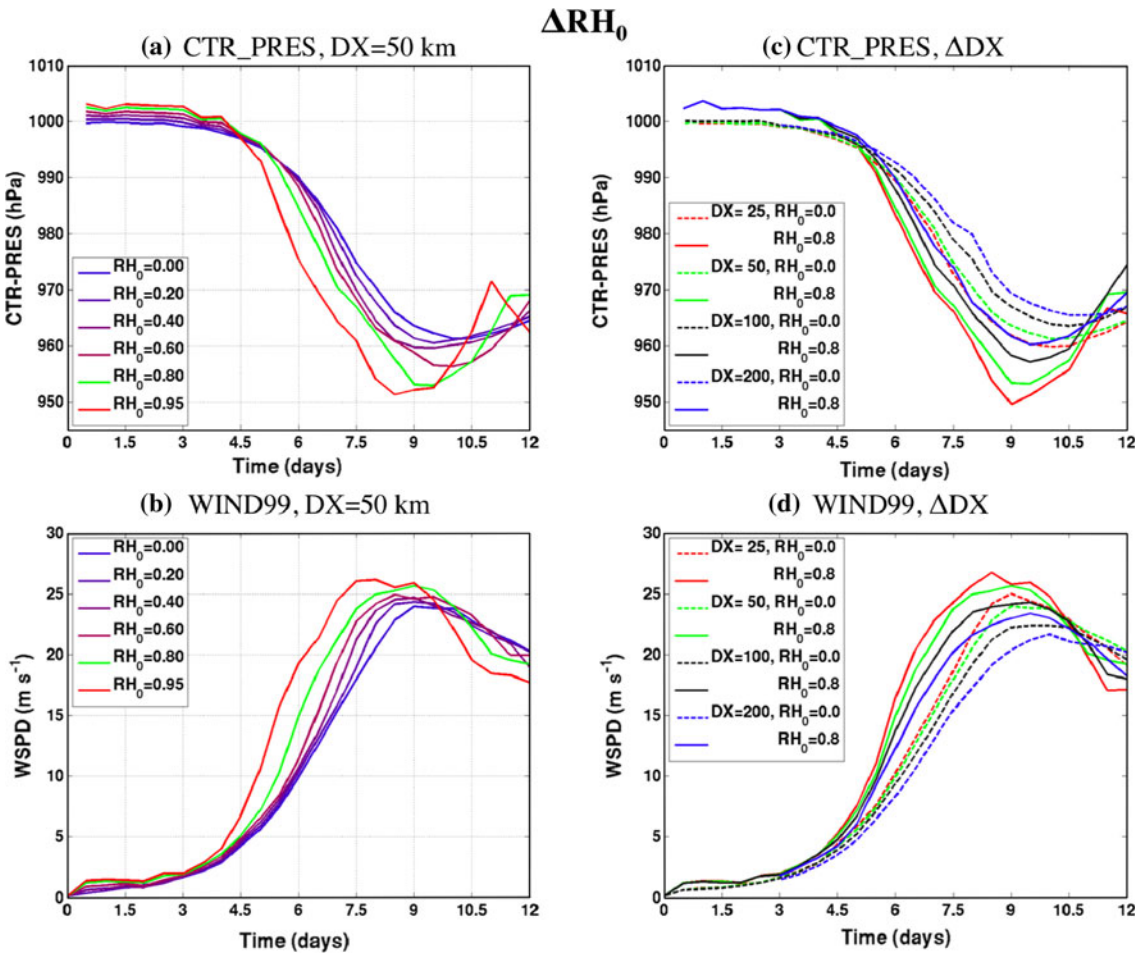

Fig. 3 Time evolution of CTR_PRES and WIND99, for the RH_0 experiment (**a**, **b**) and the integrations with different grid spacing (**c**, **d**). In all figures, the *green solid line* is the same reference integration. In (**a**, **b**), *blue* is the lowest and *red* is the highest RH_0. In (**c**, **d**), the *solid curves* show the $RH_0 = 0.8$ cases and the *dashed curves* show the cases with $RH_0 = 0$. Units for CTR_PRES: hPa, for WIND99: m/s

latent heating was turned off (e.g., ~20 hPa in Reed et al. 1993 and Stoelinga 1996). However, only the initial conditions are dry in our study, as the sea surface boundary condition acts as a continuous moisture source. This means that there is at least some latent heating in all of the storms in Fig. 3a, even for $RH_0 = 0$.

The effect of increasing the initial RH on the extremes of surface wind speed is shown in Fig. 3b, where we plot WIND99 for all the six integrations. As with central pressure, WIND99 grows faster and strengthens as the initial moisture is increased, even in the integration with $RH_0 = 0.95$. Hence, in all these related yet different quantities, moister storms develop faster and are grow stronger than dryer ones.

We again address the question of numerical resolution in Fig. 3c, d, where CTR_PRES and WIND99 are plotted for DX = 25, 20, 100 and 100 km, as in Fig. 2b. A comparison of the solid (reference RH_0) and dashed (initially dry) curves for any color shows that the moister storms have deeper central pressure minima and stronger extreme surface winds, for all values of DX (Fig. 3c, d). Thus, the moister initial conditions generates not only larger EKE, but also deeper central pressure and stronger winds, and these results are robust to changes in the grid spacing.

Finally, we turn our attention to the extreme precipitation metrics: as mentioned above, we document separately the large-scale precipitation extremes ($PRCP99_{LS}$) and the cumulus precipitation extremes ($PRCP99_{CU}$). Figure 4a, b show the time evolution for $PRCP99_{LS}$ and $PRCP99_{CU}$ for the 6 integrations in Experiment 1, at the standard resolution of DX = 50 km. Not surprisingly, the strongest large-scale and cumulus precipitation rates occur in the runs with larger RH_0. As before, Fig. 4c, d illustrate the sensitivity of these quantities to DX. In accord with the storm strength, both extreme precipitation rates increase with RH_0 for all horizontal resolutions (Fig. 4c, d).

We conclude the discussion of Experiment 1 by showing, in Fig. 5, the hourly accumulated precipitation fields

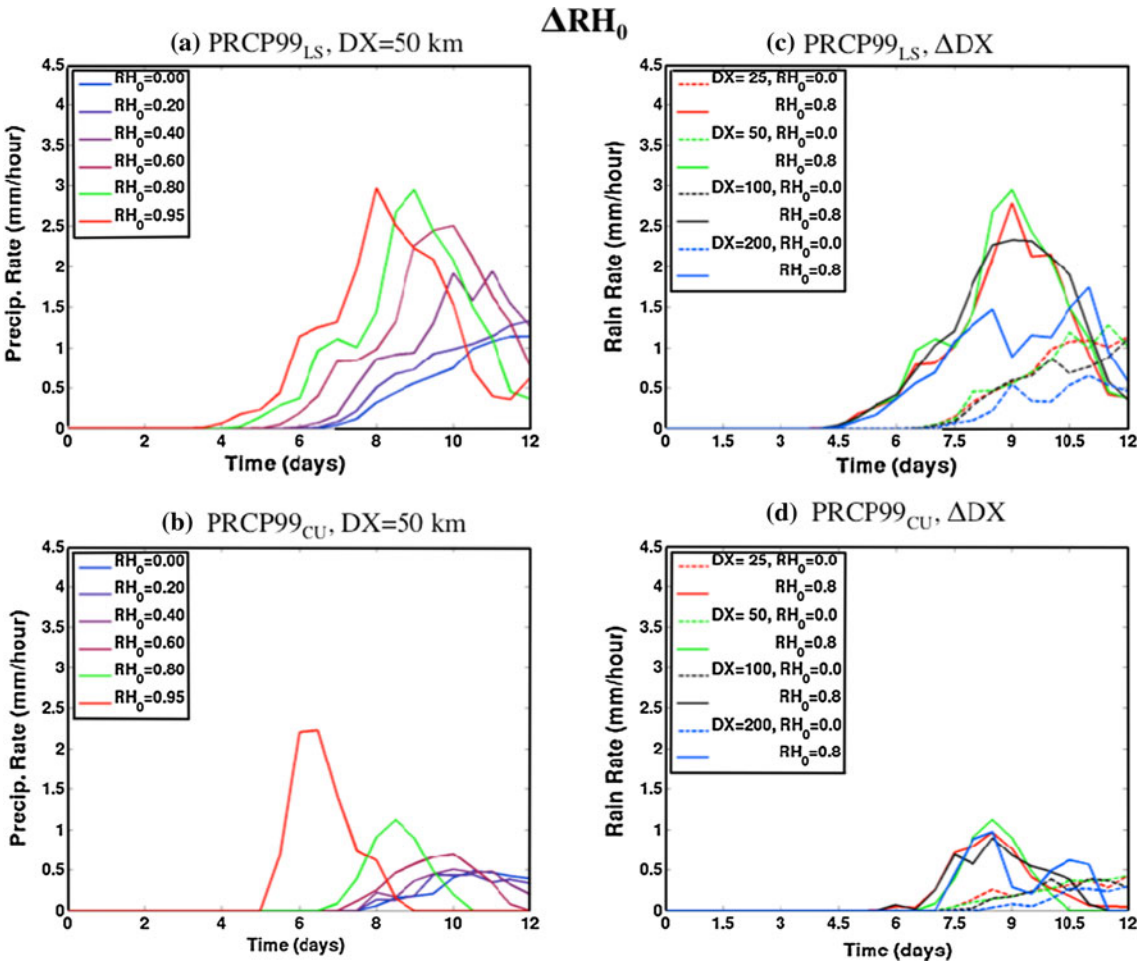

Fig. 4 Time evolution of extreme precipitation $PRCP99_{LS}$ and $PRCP99_{CU}$, for the RH_0 experiment (**a**, **b**) and the integrations with different grid spacing (**c**, **d**). In all figures, the *green solid line* is the same reference integration. In (**a**, **b**), *blue* is the lowest and *red* is the highest RH_0. In (**c**, **d**), the *solid curves* show the $RH_0 = 0.8$ cases and the *dashed curves* show the cases with $RH_0 = 0$. Units for precipitation rates: mm/hour

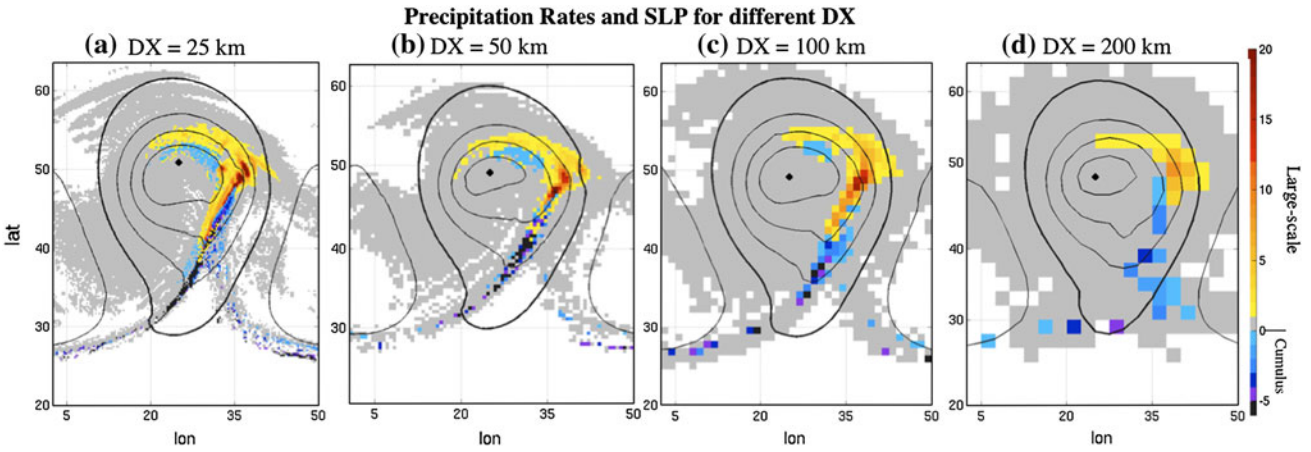

Fig. 5 Sea level pressure (*contours*) and precipitation rate (*color*) for different grid spacing (DX), shown at the time that each storm's EKE is ½ of its maximum. SLP contours increase monotonically outwards from the storm center, starting with 970 hPa, contour interval = 10 hPa. The thicker contour is 1,000 hPa. Precipitation generated by the cumulus scheme is plotted as negative. Precipitation units: mm/hour. The axes use the same convention as Fig. 1

with different DX, at the point when the storm EKE is half of EKE_{MAX}. Along the region of strong precipitation in the cyclone's warm sector, the strength of the precipitation increases as DX decreases from 200 to 100 to 50 km, but is quite similar in the models with DX = 50 and 25 km (panels a and b). In light of this, Experiments 2 and 3 were carried out using 50 km. We note that such horizontal resolution is similar to the ones in the GCM experiments analyzed by Bengtsson et al. (2009) and Catto et al. (2011).

3.2 Experiment 2: varying C_{SVP} from 0 to 1

The second and third sets of integrations examine the storm sensitivity to moisture by varying the saturation vapor pressure coefficient (C_{SVP}), as described in Sect. 2 (see Eq. 2). The advantage of doing this resides in the fact that moisture can be increased without changes in RH, in accordance with the conditions projected to occur with global warming (e.g., Sherwood et al. 2010). Also, by using this method to increase the moisture content, one avoids the complications involved in changing the temperature in the troposphere, as discussed in the introduction. For these integrations, we fix the value of RH_0 at 0.8. Thus, the integration with $C_{SVP} = 1$ is identical to the reference case described above. When $C_{SVP} = 0$, the moisture content is zero, and the atmosphere remains completely dry for the entire life cycle.

We start by considering the range $0 < C_{SVP} < 1$, termed Experiment 2 (see Table 1). This set of integrations studies the effect that increasing water vapor from completely dry to present conditions has on a midlatitude storm, using an alternate method to that of Experiment 1. It serves to validate the conclusions of Experiment 1 with a different method, and to set the stage for understanding how baroclinic lifecycles may change under future, moister conditions.

In the three panels of Fig. 6, we plot the time-evolution of the EKE, CTR_PRES and WIND99 for the integrations from Experiment 2. We plot the results for all six integrations on the same figure, using a different color for each value of C_{SVP}, from 0 to 1, in steps of 0.2. For each metric, the direction of the response to moisture is the same as Experiment 1: the storm strength increases as we increase the moisture, with an appearance of saturation in EKE near $C_{SVP} = 1$.

The take home message here is that, even when the relative humidity is kept constant, the storm becomes stronger when moisture content is increased. In Experiment 2, the storms also grow faster as moisture increases, however, the change in growth rate is not as drastic as it is Experiment 1 (e.g., Fig. 2a). This is because in Experiment 2 the time it takes for the rising air to reach saturation is nearly the same in each integration, since all have the same initial RH. Note also that the differences in storm strength between the dry and the moist integrations are larger in Experiment 2 than in Experiment 1 (e.g., compare Figs. 6a, 2a). This is because the driest storm in Experiment 2 (with $C_{SVP} = 0$) is remains completely dry throughout its life cycle, while setting $RH_0 = 0$ in Experiment 1 only sets the initial moisture to zero (but latent heating still occurs in the life cycle as moisture is added via surface evaporation).

The extreme precipitation rates for Experiment 2 are shown in Fig. 7, in the same manner as the storm strength. The large-scale precipitation $PRCP99_{LS}$ increase in step with C_{SVP} (panel a). The cumulus precipitation $PRCP99_{CU}$ also increases with moisture content, even though $PRCP99_{CU}$ is zero for $C_{SVP} < 0.6$. This is because convective instability is too weak to initiate sub-grid scale deep convection in the cases with small C_{SVP}.

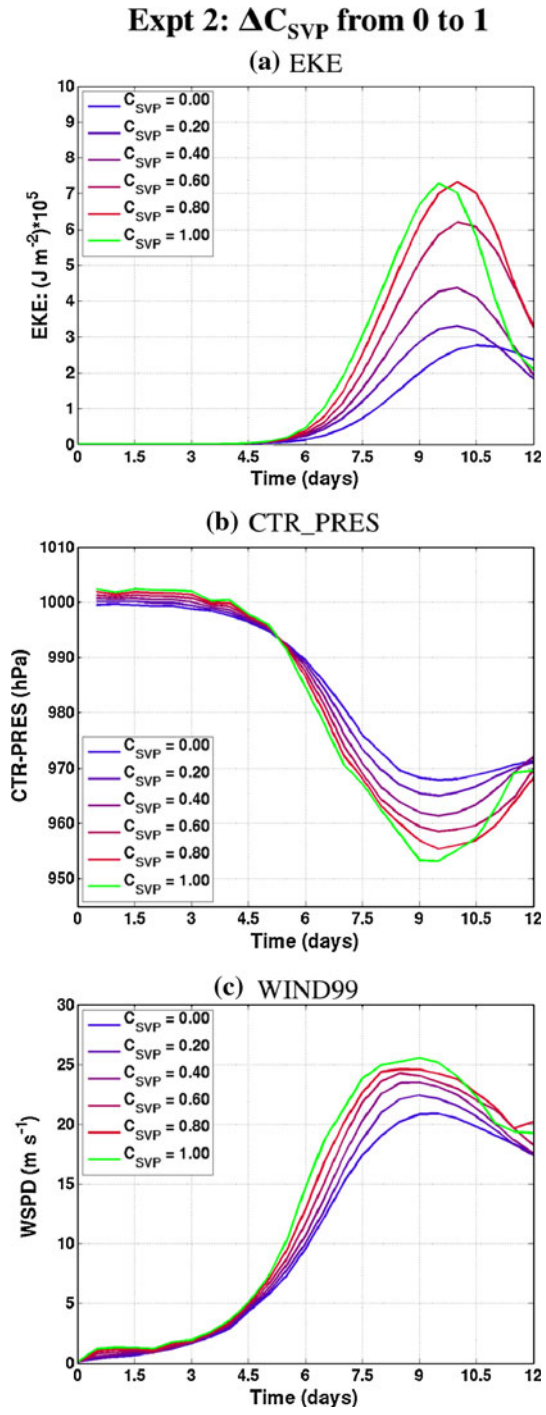

Fig. 6 Time evolution of EKE (**a**), CTR_PRES (**b**) and WIND99 (**c**) for Experiment 2. In all figures, the *green line* is the reference integration, *blues* represent smaller C_{SVP} values and *reds* represent larger C_{SVP}. Units: EKE: 10^5 J/m^2, CTR_PRES: hPa, WIND99: m/s

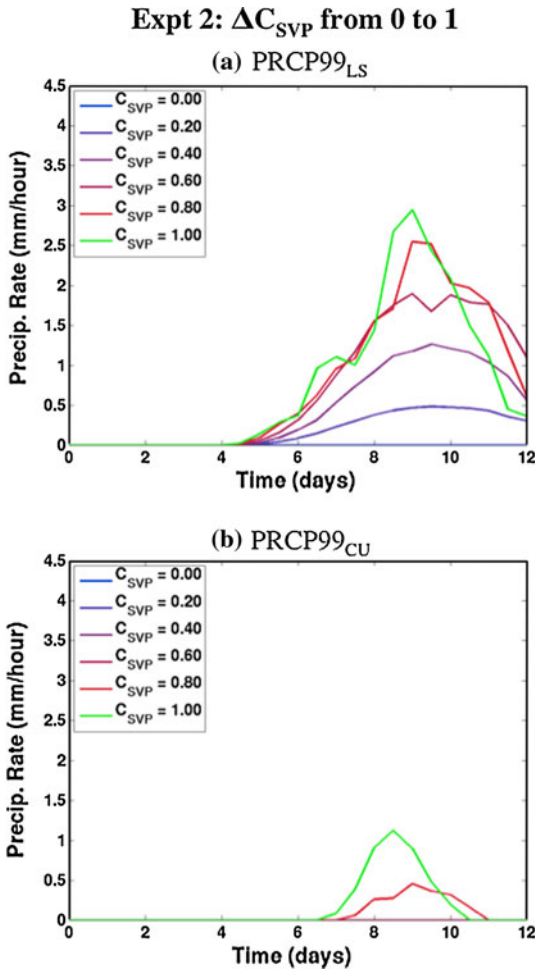

Fig. 7 Time evolution of the extreme precipitation rates at the large-scale scale, $PCPC99_{LS}$ (**a**), and from the cumulus scheme, $PCPC99_{CU}$ (**b**). In all figures, the *green line* is the reference integration, *blues* represent smaller C_{SVP} values and *reds* represent larger C_{SVP}. Units: mm/hour

In summary then, Experiment 2 shows that increasing moisture strengthens the storm and the accompanying precipitation even when the initial RH is fixed, and this result is robust across all of our storm strength metrics. The qualitative agreement between the results for Experiments 1 and 2 shows that altering the moisture content by changing C_{SVP} does not create any unexpected odd behavior, but in fact yields meaningful results. With this in mind, we now consider how the storm strength is affected when $C_{SVP} > 1$, to help understand how future global warming might affect baroclinic life cycles.

3.3 Experiment 3: varying C_{SVP} from 1 to 2

It is well established that atmospheric moisture content will increase with global warming (e.g., Held and Soden 2006), and this change should provide an increased moisture source for midlatitude storms. To quantify the projected change in moisture, we start by first calculating the change in specific humidity by 2100 for each GCM in the CMIP3 Scenario A2 (see Sect. Appendix for details on the models used and CMIP3 Scenario A2). In Fig. 8a we show both the multimodel mean 1980–2000 (black contours) and the

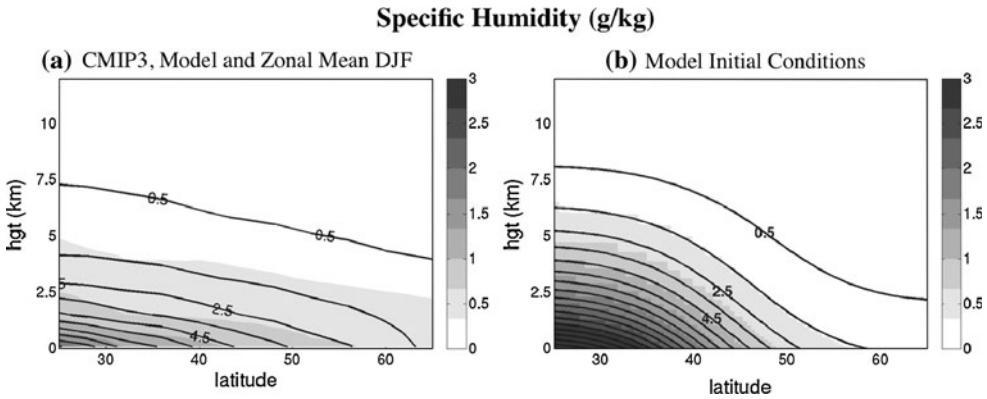

Fig. 8 Zonal mean specific humidity (*contours*) and differences (*shading*), for the CMIP3 ensemble average for winter (DJF) (**a**) and for the model (**b**). In (**a**) the contours show the 1980–2000 mean; the shading shows 2080–2100 minus 1980–2000. In (**b**), the contours show the initial conditions for $C_{SVP} = 1.0$, the shading show initial conditions for $C_{SVP} = 1.25$ minus $C_{SVP} = 1$

projected changes (i.e., the 2080–2100 mean minus the 1980–2000 mean, in color); we limit the latitudes to the domain used in our life cycle experiments. The figure shows that the change in moisture is most pronounced near the surface, at low latitudes. In agreement with these projections, varying C_{SVP} creates the largest changes in moisture near the surface in the low latitudes.

To study the impacts of the moisture increase with global warming, we create a third set of integrations, with C_{SVP} values ranging from 1 to 2 in increments of 0.2: this set will be referred to as Experiment 3 (see Table 1). As Fig. 8b illustrates, the C_{SVP} value of 1.2 creates the moisture changes that are stronger to those found in the CMIP3 (Fig. 8a). However, the CMIP3 result shows the zonal mean for all longitudes averaged over winter, while our model initial conditions represent a snapshot prior to storm formation. We also run integrations with larger values of C_{SVP} to document the storm response to larger moisture increases. Note that Frierson et al. (2006) used values of C_{SVP} as large as 10; however, we found that our model becomes numerically unstable when larger values of C_{SVP} are used.

We first consider how the dynamical metrics EKE_{MAX}, CTR_PRES and WIND99 change as C_{SVP} is increased beyond 1. Figure 9a shows that the EKE_{MAX} decreases as C_{SVP} approaches 1.4, levels off at $C_{SVP} = 1.6$ and then increases beyond that point, such that the EKE_{MAX} for $C_{SVP} = 1$ and 2 are the same. This non-monotonic response appears to be unique to the EKE, and we discuss this in Sect. 4 below. In addition, note that the changes in EKE_{MAX} for the cases with $C_{SVP} > 1$ are relatively small ($\sim$10–15 % of EKE_{MAX} in the reference integration), compared to the response found in Experiment 2 (more than 70 % of the reference case in Fig. 6a).

Unlike EKE, the central pressure deepens monotonically with C_{SVP}, with $C_{SVP} = 2$ having the deepest low (approximately 945 hPa, as seen in Fig. 9b). Similarly, the surface wind maximum increases monotonically from 25 m/s to nearly 30 m/s with C_{SVP} increasing from 1 to 2 (Fig. 9c). Thus, in Experiment 3, the CTR_PRES and WIND99 respond to the moisture increase in the same manner as they did in Experiments 1 and 2.

For the extreme precipitation rates in Experiment 3, the responses of the large-scale and cumulus precipitation differ, as illustrated in Fig. 10. The large-scale precipitation rates, $PRCP99_{LS}$, increase monotonically with C_{SVP} during the initial growth of the storm (at day 6 in Fig. 10a), but the overall maxima in $PRCP99_{LS}$, which occur around day 8.5, are very similar for all of the integrations. In contrast, the extreme precipitation from the cumulus scheme, $PRCP99_{CU}$, increases monotonically with C_{SVP} (Fig. 10b), which is in agreement with the response of the CTR_PRES and WIND99.

4 Discussion

4.1 The accumulated precipitation

Here we consider the accumulated precipitation, which includes both the large-scale and the cumulus precipitation, averaged over the entire domain and over the entire life-cycle. This metric offers a time and space integrated response of the storm to changes in moisture, and allows us to easily compare the response in the different experiments using a single quantity. Table 2 shows the accumulated precipitation for each of the integrations.

For Experiment 1, the first result to note is that the $RH_0 = 0$ case has a non-zero value. This serves as a reminder that this integration is only dry in the initial conditions. Second, as RH_0 is increased, the accumulated precipitation increases gradually, such that the reference case, $RH_0 = 0.8$, has double the accumulated precipitation of the case with $RH_0 = 0$. Finally with $RH0 = 0.95$ the accumulated precipitation increases drastically. Interestingly, this is mostly due to a large increase in the spatial extent of cumulus precipitation in the lower latitudes of the domain (not shown).

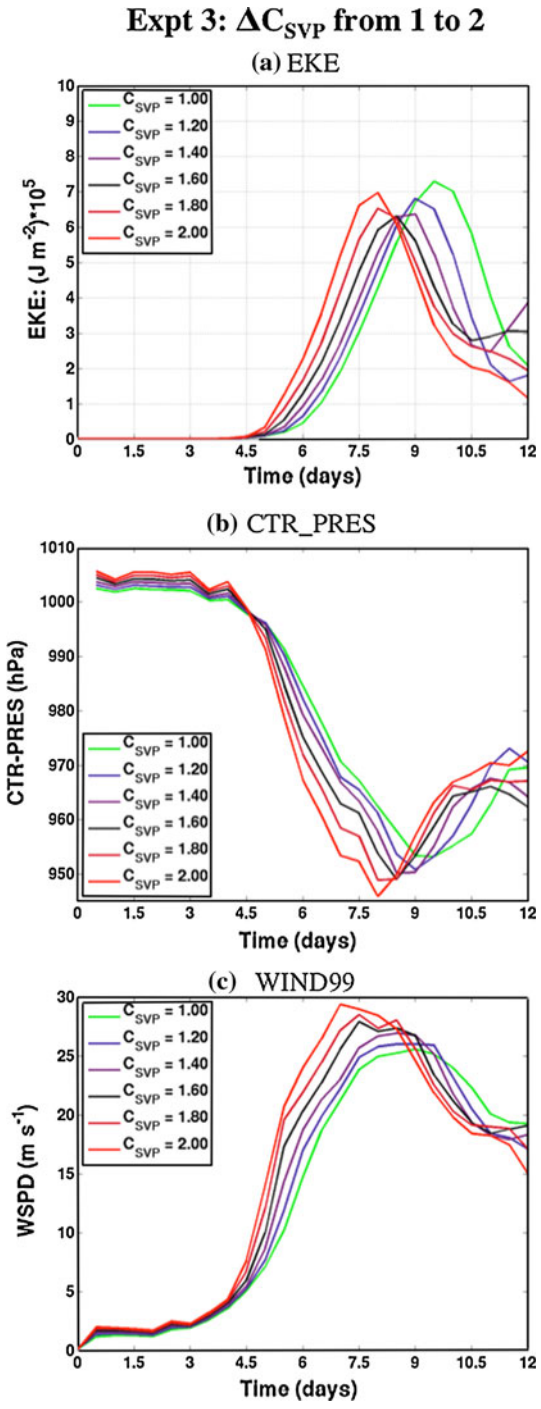

Fig. 9 Time evolution of EKE (**a**), CTR_PRES (**b**) and WIND99 (**c**) for Experiment 3. In all figures, the *green line* is the reference integration, *blues* represent smaller C_{SVP} values and *reds* represent larger C_{SVP}. The $C_{SVP} = 1.6$ integration is plotted in *black*. Units: EKE: 10^5 J/m^2, CTR_PRES: hPa, WIND99: m/s

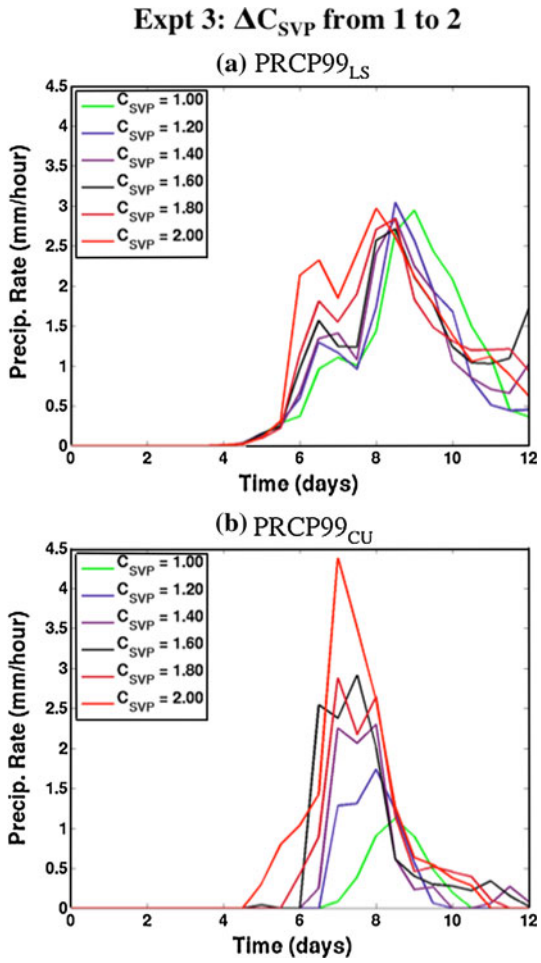

Fig. 10 Time evolution of the extreme precipitation rates at the large-scale scale, $PCPC99_{LS}$ (**a**), and from the cumulus scheme, $PCPC99_{CU}$ (**b**), for Experiment 3. In all figures, the *green line* is the reference integration, *blues* represent smaller C_{SVP} values and *reds* represent larger C_{SVP}. The $C_{SVP} = 1.6$ integration is plotted in *black*. Units: mm/hour

In Experiment 2, the accumulated precipitation appears to increase even more rapidly with increasing C_{SVP} (except with $RH_0 = 0.95$, which is exceptional). Note, however, that the values of accumulated precipitation are here smaller than in Experiment 1: since the moisture content in the C_{SVP} integrations is limited throughout the lifecycle whereas, in the RH_0 integrations, surface evaporation provides a continuous moisture source during storm development. Thus, based on the accumulated precipitation, the $RH_0 = 0$ life cycle would be approximately equivalent to the integration in Experiment 2 with $C_{SVP} = 0.5$.

In Experiment 3, the accumulated precipitation continues to rise with C_{SVP}. This is a consequence of an increase in precipitation at both the cumulus- and large-scale (not shown). Note that, for the large-scale precipitation, this result is different from the response of the extreme precipitation rates (Fig. 10), which appeared to be largely insensitive to C_{SVP}. The conclusion, therefore, is that the change in accumulated large-scale precipitation is caused by an increase in the spatial extent of moderate precipitation rates, rather than the extremes.

Table 2 Domain-averaged accumulated precipitation (mm)

Experiment 1		Experiment 2		Experiment 3	
RH_0	Total precipitation	C_{SVP}	Total precipitation	C_{SVP}	Total precipitation
0	6.2	0	0	1	12.5
0.2	7.6	0.2	2.2	1.2	13.3
0.4	9.5	0.4	4.9	1.4	14.9
0.6	11.7	0.6	8.5	1.6	17.0
0.8	12.5	0.8	11.3	1.8	19.1
0.95	20.4	1	12.5	2	20.9

4.2 Horizontal and vertical scales

In Experiment 3, it was found that the EKE_{MAX} responds non-monotonically to increasing C_{SVP} (Fig. 9a); this behavior contrasts that of the other metrics we have considered, all of which grow monotonically with increasing moisture. To shed light on this unique EKE response, we first introduce a new metric that reflects the volume integrated wind field: the total kinetic energy (TKE). The TKE is calculated in the same manner as the EKE, but the full winds are used in the mass weighted integral.

Figure 11a, b show TKE for Experiments 2 and 3. Clearly, TKE increases monotonically with moisture across both experiments, i.e., for C_{SVP} increasing from 0 all the way up to 2. Thus, the moisture response of TKE is qualitatively similar to the other metrics. The monotonic increase of TKE indicates that more kinetic energy is converted from potential energy with increased moisture: however, the non-monotonic increase of EKE suggests that only a fraction is converted to eddy kinetic energy. Clearly, an analysis of the energy cycle is needed for further clarification, a task beyond the scope of this study. However, the response of the EKE also manifests itself in changes in the structure of the storm, which we next discuss.

Consider first the sea-level pressure field, shown by the black contours in Fig. 12, for the integrations with $C_{SVP} = 1$ (panel a) and $C_{SVP} = 2$ (panel b). Comparing the 1,000 hPa isobar (thick black contour), it is clear that the meridional extent of the storm decreases, as C_{SVP} is changed from 1 to 2. This contraction is intimately related to the non-monotonic behavior or EKE (Fig. 9a), since the EKE measures the asymmetry of the circulation with respect to the zonal mean.

In contrast to the horizontal scale, the vertical scale of the storm is found to increase with moisture monotonically. To show this we analyze the vertical profile of the wind field, and plot WIND99 versus height, in Fig. 13, for the integrations in Experiments 2 and 3. These extreme wind profiles are calculated at the times when each storm reaches an EKE value that is half of it own maximum EKE. Across the two experiments, the height of the wind maximum increases with C_{SVP}. We interpret this as an increase in the vertical height of the cyclone. We reach the same conclusion after analyzing the height of the tropopause (not shown here), in the region of the storm located between the warm front and the cold front and above the location of maximum precipitation.

Understanding the response of the storm's horizontal and vertical scales to increased moisture is still elusive. Previous theoretical studies have found that increasing moisture leads to an excitation of a smaller length scales (e.g., Emanuel et al. 1987), and this might explain the change in horizontal scale documented above in our integrations. However, the same theories predict that the vertical scale of the storm should also decrease. Hence it is not clear how to reconcile those earlier theories with our results.

Even more perplexing are the findings of Frierson et al. (2006), who recently addressed these same question (in the context of an idealized GCM) by varying C_{SVP} as we have done. They found only a small change in the horizontal

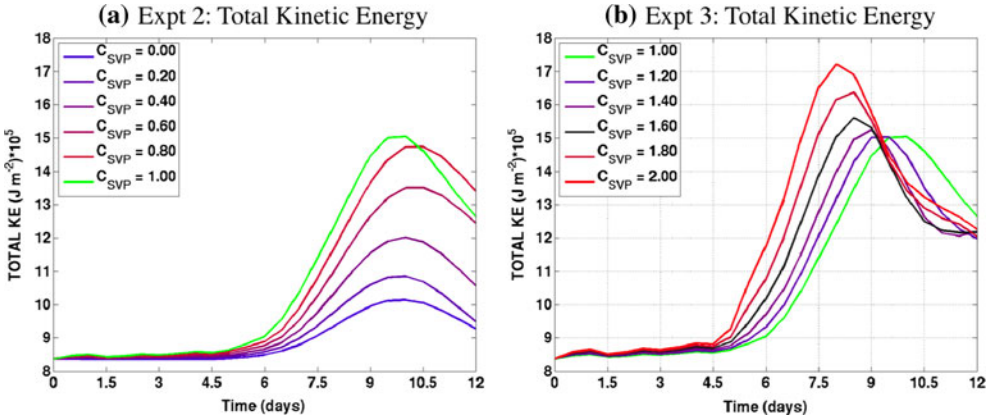

Fig. 11 Time evolution of TKE for Experiment 2 (**a**) and Experiment 3 (**b**). The *green curve* is the reference integration, *blues* represent smaller C_{SVP} values and *reds* represent larger C_{SVP} values. The case with $C_{SVP} = 1.6$ is shown in *black*. Units: 10^5 J/m^2

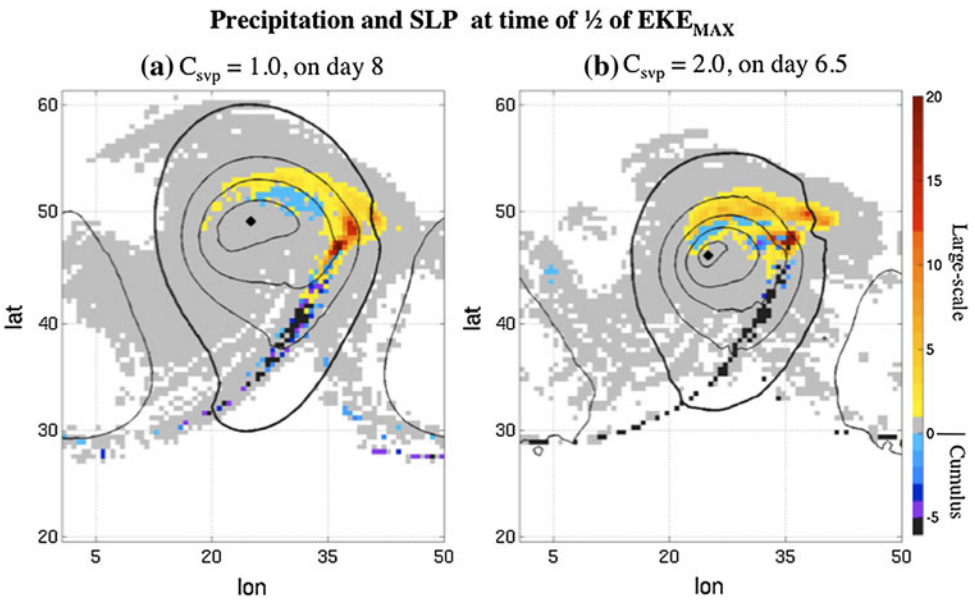

Fig. 12 Sea level pressure (*contour*) and precipitation rate (*color*), for the integration with $C_{SVP} = 1$ (**a**) and $C_{SVP} = 2$ (**b**). The storms are shown at time when EKE is half of each storm's EKE_{MAX}: this corresponds to day 8 for (**a**) and day 6.5 for (**b**). SLP contours increase monotonically outwards from the storm center, contour interval = 10 hPa. The thicker contour is 1,000 hPa. Precipitation generated by the cumulus scheme is plotted as negative. Precipitation units: mm/hour. The axes use the same convention as Fig. 1

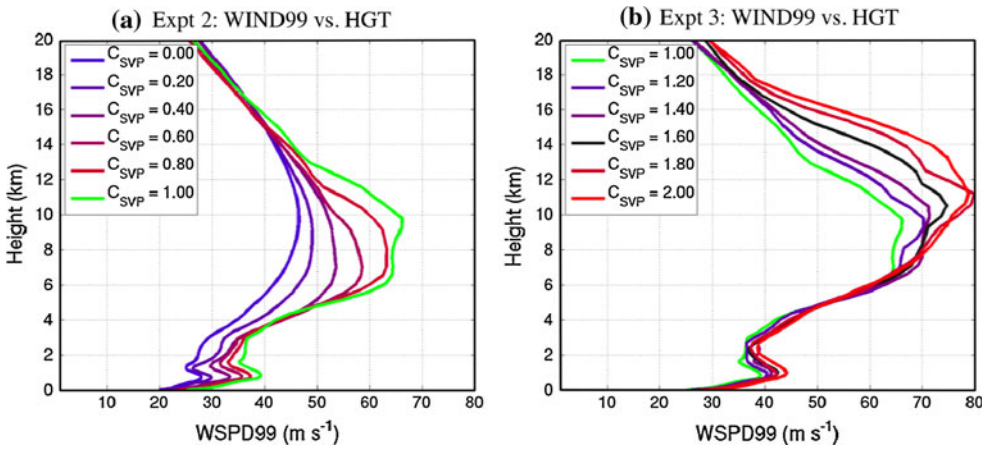

Fig. 13 Time evolution of WIND99 versus height for Experiment 2 (**a**) and Experiment 3 (**b**). The *green curve* shows the reference integration, *blues* represent smaller C_{SVP} values and *reds* represent larger C_{SVP} values. The case with $C_{SVP} = 1.6$ is shown in *black*. Units: m/s

eddy length-scale when varying C_{SVP} over a much broader range than we have done here. They suggest that the most likely explanation for the small length scale changes in their model might be due to a shift in the latitude of their model's subtropical jet, an explanation that does not immediately seem applicable to our results, since we use the same initial winds in all integrations.

In summary then, the response of midlatitude storms' length scales as moisture is increased remains an open question. Nonetheless, as we have amply documented above, the response to increasing moisture in all other important metrics (notably wind speed and precipitation) is clear and robust: as moisture is increased the storm becomes stronger.

5 Summary and conclusion

The purpose of this study has been to examine the response of midlatitude storms to increases in moisture content, a scenario expected under the global warming. Three numerical experiments with idealized baroclinic life cycles were carried out. The first one examined the storm response to different initial relative humidity. In the second and third ones the initial RH was held fixed, and moisture content was varied using the coefficient C_{SVP} in the Clausius-Clapeyron equation, either from dry to present conditions, or for present to future conditions.

The main, robust result that emerges from these experiments is that as moisture is increased nearly all the important metrics of storm strength increase. Specifically the storm's intensification rate, central pressure minimum, extreme surface winds and precipitation, increases monotonically with moisture. We have also verified that these conclusions are robust to changes in the model's horizontal grid size, including models with a relatively coarse resolution, typical of current generation models used for climate change projections. This suggests that the storm enhancement associated with increased moisture can be

captured even when the rising motion within the storm's warm sector and the individual fronts are not well resolved.

In addition, we found that increasing moisture beyond current levels (as in Experiment 3) results in storms that are smaller in size, even though the storm's strength, as measured by the central pressure or extremes of the surface winds and precipitation increase. While increasing moisture reduces the horizontal scale of the storm it also helps generate more vigorous rising motion in the warm sector, which causes the height of the storm to increase. Whether similar behavior can be found in model output from climate change projections using state-of-the-art general circulation models remains an open question (Kidston et al. 2010; Barnes and Hartmann 2012).

In terms of the global warming projections, our results suggest that the moisture forcing on storms will not have a huge impact for the strongest storms. First, the increase in moisture in GCMs projections is weaker than the change caused by using the C_{SVP} value of 1.2 in our Experiment 3 (Fig. 8). Second, for that integration we find only modest differences (less than 10 %) in EKE, CTR_PRES or WIND99, as compared to $C_{SVP} = 1$. Hence this study suggests that increases in the moisture content under global warming could only lead to a relatively small strengthening of the midlatitude storms. This is in agreement with the GCM results reported by Bengtsson et al. (2009) and Catto et al. (2011), who found no increase in the frequency, or strength, of extreme storms in global warming projections.

We intentionally limited the scope of this study to moisture in the atmosphere, to allow for a focused examination of the impact of that one variable on midlatitude storms. Thus, by design our study cannot fully answer the question: will the strength of midlatitude storms increase with global warming? However, our study does provide one important piece needed to answer that question. Needless to say, increasing surface temperatures, changing static stabilities at different latitudes, stratospheric process and other variables are likely to affect midlatitude storms in the future. We hope to report on some of these aspects in future papers.

Acknowledgments We acknowledge the World Climate Research Programme's Working Group on Coupled Modeling, which is responsible for CMIP, and we thank the climate modeling groups (listed in the Sect. Appendix) for producing and making available their model output. For CMIP the U.S. Department of Energy's PCMDU provides coordinating support and led development of software infrastructure in partnership with the Global Organization for Earth System Science Portals. The work of LMP is funded, in part, by a grant from the US National Science Foundation. The work of JFB is funded by the National Aeronautics and Space Administration (NASA) postdoctoral program. SW thanks Jian Lu for discussions of experiment design at earlier phase. We thank Heini Wernli and an anonymous reviewer for useful suggestions that helped to clarify the presentation of the main points of this work.

Appendix: Details for Fig. 8

For Fig. 8, we download data from the Program for Climate Model Diagnosis and Intercomparison (PCMDI), CMIP3 archive for the IPCC AR4. We use the historical model integrations to represent the twentieth century and the runs from the Global Warming A2 scenario for the twentyfirst century. Scenario A2 from CMIP3 corresponds to an increase in global temperatures in the range from 2–5 °C. The increase in CO_2 associated with this scenario seemed pessimistic when it was created in 2000, but not anymore. We chose Scenario A2 because it corresponds to a projection in which economies maintain the status quo, which doesn't seem unreasonable.

Models used in Fig. 8

BCCR: Bergen Climate Model (BCM) project at the Bjerknes Centre for Climate Research. CCCMA: Canadian Centre for Climate Modeling and Analysis, Victoria, BC, Canada. CCSM: Community Climate System Model project, supported by the, Directorate for Geosciences of the National Science Foundation, and the Office of Biological and Environmental Research of the U.S. Department of Energy. CNRM: Centre National de Recherches Meteorologiques, Meteo-France, Toulouse, France. CSIRO: Atmospheric Research, Melbourne, Australia. ECHAM: Max Planck Institute for Meteorology, Hamburg, Germany. GFDL: US Dept of Commerce/NOAA/Geophysical Fluid Dynamics Laboratory, Princeton, NJ, USA. GISS ModelE: NASA Goddard Institute for Space Studies New York, NY, USA. INMCM: Institute for Numerical Mathematics, Moscow, Russia. IPSL: Institut Pierre Simon Laplace, Paris, France. CCSR/NIES/FRCGC: Center for Climate System Research, Tokyo, Japan/National Institute for Environmental Studies, Ibaraki, Japan/Frontier Research Center for Global Change, Kanagawa, Japan. MRI: Meteorological Research Institute, Tsukuba, Ibaraki, Japan. PCM: National Center for Atmospheric Research, Boulder, CO, USA.

References

Barnes EA, Hartmann DL (2012) The global distribution of atmospheric eddy-length scales. J Clim 25:3409–3416

Bengtsson L, Hodges KI, Keenlyside N (2009) Will extratropical storms intensify in warmer climate? J Clim 22:2276–2301

Booth JF, Thompson L, Patoux J, Kelly KA (2012) Sensitivity of midlatitude storm intensification to perturbations in the sea surface temperature near the Gulf stream. Mon Weather Rev 140:1241–1256

Boutle IA, Beare RJ, Belcher SE, Brown AR, Plant RS (2010) The moist boundary layer under a mid-latitude weather system. Boundary Layer Meteorol 134:367–386

Boutle IA, Belcher SE, Plant RS (2011) Moisture transport in mid-latitude cyclones. Q J R Meteorol Soc 137:360–367
Campa J, Wernli H (2012) A PV perspective on the vertical structure of mature midlatitude cyclones in the Northern Hemisphere. J Atmos Sci 69:725–740
Carlson TN (1998) Mid-Latitude weather systems. American Meteorological Society, Boston
Catto JL, Shaffrey LC, Hodges KI (2011) Northern Hemisphere extratropical cyclones in a warming climate in the HiGEM high-resolution climate model. J Clim 24:5336–5352
Champion AJ, Hodges KI, Bengtsson LO, Keenlyside NS, Esch M (2011) Impact of increasing resolution and a warmer climate on extreme weather from Northern Hemisphere extratropical cyclones. Tellus 63A:893–906
Chen S-H, Sun W-Y (2002) A one-dimensional time dependent cloud model. J Meteorol Soc Jpn 80:99–118
Davis CA, Stoelinga MT, Kuo Y-H (1993) The integrated effect of condensation in numerical simulations of extratropical cyclogenesis. Mon Weather Rev 121:2309–2330
Emanuel KA, Fantini M, Thorpe AJ (1987) Baroclinic instability in an environment of small stability to slantwise moist convection. Part I: two-dimensional models. J Atmos Sci 44:1559–1573
Fantini M (1993) A numerical study of two-dimensional moist baroclinic instability. J Atmos Sci 50:1199–1210
Frierson DMW, Held IM, Zurita-Gotor P (2006) A gray-radiation aquaplanet moist GCM. Part 1: static stability and eddy scale. J Atmos Sci 63:2548–2566
Gastineau G, Soden BJ (2009) Model projected changes of extreme wind events in response to global warming. Geophys Res Lett 36:L10810. doi:10.1029/2009GL037500
Gutowski WJ, Branscome LE, Stewart DA (1992) Life cycles of moist baroclinic eddies. J Atmos Sci 49:306–319
Held IM, Soden BJ (2006) Robust responses of the hydrological cycle to global warming. J Clim 19:5686–5699
Holton JR (2004) An introduction to dynamic meteorology, 4th edn. Elsevier Academic, New York
Hong S-Y, Noh Y, Dudhia J (2006) A new vertical diffusion package with an explicit treatment of entrainment processes. Mon Weather Rev 134:2318–2341
Kain JS, Fritsch JM (1993) Convection parameterization for mesoscale models: the Kain-Fritsch scheme. In: Emanuel KA, Raymond DJ (eds) The representation of cumulus convection in numerical models. Amer Meteor Soc, Boston
Kidston J, Dean SM, Renwick J, Vallis GK (2010) A robust increase in the eddy length scale in the simulation of future climates. Geophys Res Lett 37:L03806
Lambert SJ, Fyfe JC (2006) Changes in winter cyclone frequencies and strengths simulated in enhanced greenhouse warming experiments: results from the models participating in the IPCC diagnostic exercise. Clim Dyn 26:713–728
Li F, Collins WD, Wehner MF, Williamson DL, Olson JG (2011) Response of precipitation extremes to idealized global warming in an aqua-planet climate model: towards a robust projection across different horizontal resolutions. Tellus 63A:876–883
Lin Y-L, Farley RD, Orville HD (1983) Bulk parameterizations of the snow field in a cloud model. J Clim Appl Meteorol 22:1065–1092
Lorenz DJ, DeWeaver ET (2007) Tropopause height and zonal wind response to global warming in the IPCC scenario integrations. J Geophys Res 112:D10119. doi:10.10292006JD008087
Mak M (1994) Cyclogenesis in a conditionally unstable moist baroclinic atmosphere. Tellus 46A:14–33
Martin J (2006) Mid-latitude atmospheric dynamics. Wiley, West Sussex
Naud CM, Del Genio AD, Bauer M, Kovari W (2010) Cloud vertical distribution across warm and cold fronts in CloudSat–CALIPSO data and a general circulation model. J Clim 23:3397–3415
O'Gorman PA, Schneider T (2009) The physical basis for increases in precipitation extremes in simulations of 21st-century climate change. Proc Natl Acad Sci 106:14773–14777
O'Gorman PA (2011) The effective static stability experienced by eddies in a moist atmosphere. J Atmos Sci 68:75–90
Pavan V, Hall N, Valdes P, Blackburn N (1999) The importance of moisture distribution for the growth and energetics of baroclinic eddies. Ann Geophys 17:242–256
Polvani LM, Esler JG (2007) Transport and mixing of chemical air masses in idealized baroclinic life cycles. J Geophys Res 112:D23102. doi:10.1029/2007JD008555
Reed RJ, Grell G, Kuo Y-H (1993) The ERICA IOP 5 storm. Part II: sensitivity tests and further diagnosis based on model output. Mon Weather Rev 121:1595–1612
Rotunno R, Skamarock WC, Snyder C (1994) An analysis of frontogenesis in numerical simulations of baroclinic waves. J Atmos Sci 51:3373–3398
Sherwood SC, Roca R, Weckwerth TM, Andronova NG (2010) Tropospheric water vapor, convection and climate. Rev Geophys 48:2009RG000301
Simmons AJ, Hoskins BJ (1978) The life cycles of some non-linear baroclinic waves. J Atmos Sci 35:414–432
Skamarock WC, Klemp JB, Dudhia J, Gill DO, Barker DM, Duda M, Huang X-Y, Wang W, Powers JG (2008) A description of the advanced research WRF Version 3, NCAR Technical Note http://www.mmm.ucar.edu/people/skamarock/
Solomon S, Qin D, Manning M, Chen Z, Marquis M, Averyt KB, Tignor M Miller HL (eds) (2007) Climate change 2007: the physical science basis. In: Contribution of working group i to the fourth assessment report of the intergovernmental panel on climate change. Cambridge University Press, New York
Stoelinga MT (1996) A potential vorticity-based study on the role of diabatic heating and friction in a numerically simulated baroclinic cyclone. Mon Weather Rev 124:849–874
Thorncroft CD, Hoskins BJ, McIntyre ME (1993) Two paradigms of baroclinic wave life-cycle behaviour. Q J R Meteorol Soc 119:17–55
Ulbrich U, Leckebusch GC, Pinto JG (2009) Extra-tropical cyclones in the present and future climate: a review. Theor Appl Climatol 96:117–131
Wang S, Polvani LM (2011) Double tropopause formation in idealized baroclinic life cycles: The key role of an initial tropopause inversion layer. J Geophys Res 116:D05108. doi:10.1029/2010JD015118
Weisman ML, Klemp JB (1982) The dependence of numerically simulated convective storms on vertical wind shear and buoyancy. Mon Weather Rev 110:504–520
Wernli H, Davies HC (1997) A Lagrangian based analysis of extratropical cyclones: the method and some applications. Q J R Meteorol Soc 123:467–490
Whitaker JS, Davis CA (1994) Cyclogenesis in a saturated environment. J Atmos Sci 51:889–907